Process variation in Laser Powder Bed Fusion of Ti-6Al-4V

Additive Manufacturing 41 (2021) 101987

Contents lists available at ScienceDirect

Additive Manufacturing

journal homepage: www.elsevier.com/locate/addma

Process variation in Laser Powder Bed Fusion of Ti-6Al-4V

Zhuoer Chen [a,b,c,*], Xinhua Wu [c,d], Chris H.J. Davies [b,c]

[a] Department of Industrial and Materials Science, Chalmers University of Technology, Gothenburg 412 96, Sweden
[b] Department of Mechanical and Aerospace Engineering, Monash University, Clayton, VIC 3800, Australia
[c] Monash Centre for Additive Manufacturing, 11 Normanby Road, Notting Hill, VIC 3168, Australia
[d] Department of Materials Science and Engineering, Monash University, Clayton, VIC 3800, Australia

ARTICLE INFO

Keywords:
Laser Powder Bed Fusion
Process variation
Qualification
Surface roughness

ABSTRACT

In this work, a concept of using surface roughness data as an evaluation tool of the process variation in a commercial Laser Powder Bed Fusion (L-PBF) machine is demonstrated. The interactive effects of powder recoating, spatter generation, gas flow and heat transfer are responsible for the intra-build quality inconsistency of the L-PBF process. Novel specimens and experiments were designed to investigate how surface roughness varies across the build volume and with the progression of a build. The variation in roughness has a clear and repeatable pattern due to the strong impact of the orientation of inclined surface to the laser origin. The effects of other factors such as exposure sequence of specimens, build height, and recoating process are less prominent and are difficult to isolate. A neural network regression model was built upon the large dataset in measured Ra values. The neural network model was applied to predict distribution of roughness within the build volume under hypothetical processing conditions. Connections between the predicted variation in roughness and underlying physical mechanisms are discussed. The present work has value for machine qualification and modifications which lead to the manufacturing of parts with better consistency in quality. The detailed variation observed in surface roughness can be used as a reference for designing experiments to optimise processing parameters in order to minimise the roughness of inclined surfaces.

1. Introduction

Laser Powder Bed Fusion (L-PBF) uses a focused laser beam to selectively fuse thin layers of metal powder according to cross-sectional profiles of three-dimensional (3D) computer-aided designs. L-PBF produced parts is currently qualified through trial-and-error experiments [1], while various simulation tools, combined with experiments, can assist to reduce the time and cost for the qualification process [2]. Quality assurance at part level requires good knowledge of the various sources of variations in part qualities. The characteristics of the feedstock powder [3] and its interaction with the powder delivery system introduce one source of the process variation by affecting the quality of powder coating, i.e. the effective layer thickness, the packing fraction and the areal coverage over the build platform [4]. Raking, rolling, or gravitational feeding of powder are all used by different L-PBF machine systems [5] and each method has its advantages and disadvantages. The size and shape distribution of the powder feedstock evolves as it is progressively recycled and new powder is added [3,6]. This in turn influences the granulometry, morphology and surface chemistry of the powder and the resultant flowability, and thus affects the performance of powder during the recoating process [4,7].

The generation of spatter, metal vapour, and plasma during laser beam interaction with metal powder [8] also contribute to the process variation. Spattering is the ejection of metal particle(s) from the melt pool due to the convective fluid flow within the melt pool and the recoil pressure exerted by evaporation [9]. Meanwhile, the intensive evaporation in the melt pool generates an inward flow of ambient gas above the melt pool that is strong enough to entrain powder particles surrounding the scan track [8]. The particles so-entrained can then be incorporated within the melt pool or ejected in any direction with respect to the laser scan direction [8] only to re-deposit on the powder bed if not carried away by the shielding gas flow [10]. As a result, the powder bed surrounding the laser scan track is disturbed and depleted of powder particles, rendering a powder denudation zone [11]. The long-range movement of spatter and entrained particles results in significant increase of actual layer thickness both locally and globally compared to the initial levelling height [12,13]. Laser scanning over the powder denudation zone or areas with re-deposited particles embeds

* Corresponding author at: Department of Industrial and Materials Science, Chalmers University of Technology, Gothenburg 412 96, Sweden.
E-mail address: zhuoer.chen@chalmers.se (Z. Chen).

https://doi.org/10.1016/j.addma.2021.101987
Received 6 October 2020; Received in revised form 26 January 2021; Accepted 24 March 2021
Available online 30 March 2021

changes in thermo-physical conditions as the laser beam melts different combinations of powder and previously solidified metal, resulting in variable surface morphology [10]. In addition, the presence of the process by-products (spatter, ejected particles, metal vapour condensates) in the laser beam path can result in energy absorption, reflection and scattering [10].

The shielding gas flow is a crucial factor of quality control during the L-PBF process. It performs three functions: (1) it provides inert atmosphere to prevent reaction between the processed metal and reactive gases [14]; (2) it directs process by-products towards the gas outlet [10]; (3) it assists cooling of the powder bed surface [15]. At a given position on the build plate, the optimum flow velocity is when metal vapour condensate is efficiently removed without disturbance of the powder bed [16]. Directed gas flow of uniform and sufficient flow velocity across the build area is beneficial for consistent part quality [10], but is difficult to achieve in practice. Commercial L-PBF machines employ different designs of gas flow systems, yielding different flow patterns over the build area [10,12] and hence produce different variations in quality attributes such as porosity, surface topology and part strength. Insufficient removal of process by-products at local areas of a build chamber due to the reduction in flow velocity results in beam attenuation and scattering, which in turn leads to a wider scan track [10], lack-of-fusion porosity [10,16], lower compression strength [16], and lower ultimate tensile strength [17]. Additionally, laser scanning in the opposite direction to the gas flow encounters less interactions between laser beam and spatter particles in comparison to the case where the laser scans along the gas flow [17]. High speed camera observations [18] suggest that the spatter particles are mainly ejected backward along the scan direction or vertically upwards, therefore when the laser travels in the same direction as the gas flow, the spatter particles are directed towards the laser beam path by the shielding gas leading to a larger beam attenuation.

Furthermore, the different thermal properties of powder compared to its solid metal counterparts make the local heat dissipation dependent on part geometry. During the L-PBF process, the melt pool can be surrounded by powder which has substantially lower effective thermal conductivity than the solid metal [19]. Therefore, heat accumulates in the vicinity of the melted area in structures like thin walls [15,20], overhangs [21], and areas built on fragmented support [22] where the heat conduction pathway through solid metal is limited. The accumulated heat leads to quality issues such as thermal warping [23] and increased surface roughness [20].

The roughness of L-PBF product surface in as-built state necessities post-processing such as polishing and machining, when the surface finish is critical to the part performance such as heat transfer and fluid flow in gas turbines [24] and fatigue life [25]. Meanwhile, The state of an as-built surface can yield valuable information about the process stability [26]. The top surface (horizontal) is the last layer processed by the laser, and can tell us about liquid metal flow and evaporation within the melt pool [27], and show traces of spatter particle redeposition and beam attenuation [10]. The side surface (vertical) shows the re-melting and wetting of consecutive layers [28]. In addition, heat input during laser scanning [29] and heat accumulation effect due to insufficient cooling of surrounding powder bed [20] can be inferred from the amount of adhered powder particles. Inclined surfaces, both upskin (upward-facing surfaces) and downskin (downward-facing surfaces) are influenced by the staircase effect, which is inherent to the layer-wise construction of additive manufactured products [30]. The staircase effect is controlled by the step size between layers, which is inversely proportional to inclination angle to the build plate (θ) and proportional to the layer thickness. The roughness of the upskin is also controlled by the re-melting and wetting between layers and the size and amount of adhered powder at layer boundaries [30]. The downskin surfaces, also referred to as overhanging surfaces, are created while the fusion zone is directly above powder bed, which has higher absorptivity [31] and lower thermal conductivity [19] compared to solid metal. Therefore, larger size of melt pools at the downskin become the dominant factor in surface roughness due to the high heat input and slow heat dissipation [21]. In the case of small inclination angle (generally $\theta < 45^{\circ}$) and excessive laser energy input, downskin surfaces develop severe thermal warpage over several deposition layers and this eventually interrupts the process due to collision between a raised edge and the recoater arm [23].

In this work, the experiment is conducted with specimens placed at nine discrete locations on the build plate that are expected to encounter different gas flow and powder recoating conditions. The specimen geometry, along with their placement and orientation in a build chamber and the order in which they are exposed by the laser beam, are designed to study multiple L-PBF process-related effects on the surface roughness of the products. These effects include the orientation of inclined surfaces to the build plate, the build-up orientation to the centre of the build chamber where the laser originates from, the location and exposure order of specimens and the build height. The result shows a clear pattern of change in average surface roughness (Ra) value with the surface orientation to the centre of the build. Inclined surfaces that were built up away from the centre of the build exhibited higher roughness compared to those built up and towards the centre, this is in agreement with the works reported previously [32–34]. In addition, local variations are found along the path of gas flow and powder recoating. The dataset was used to construct a regression model using a neural network tool. The neural network model was applied to investigate how surface roughness and its distribution over the build volume is influenced by an arbitrary perturbation to the processing conditions such as changed exposure sequence, build height, and orientation to the centre of the build platform.

2. Methodology and experimental procedure

2.1. Feedstock powder

The feedstock powder used for the current study is gas atomised Ti-6Al-4V powder with chemical composition (wt%) of 5.84Al–4.0V–0.013C–0.004N–0.003H–0.098Fe-bal.Ti. The powder was sieved to below 63 μm before it was loaded into the dispenser chamber. The sieved powder has D10, D50 and D90 of 16 μm, 30 μm and 50 μm according to size distribution tests conducted by laser diffraction technique using a Mastersizer 2000. The powder particle size distribution is plotted in Fig. 1.

2.2. The L-PBF process

The L-PBF process was carried out using an EOS M280 machine. Before the build process commenced the process chamber was flooded with argon gas until the oxygen level was lower than 1000 ppm. The

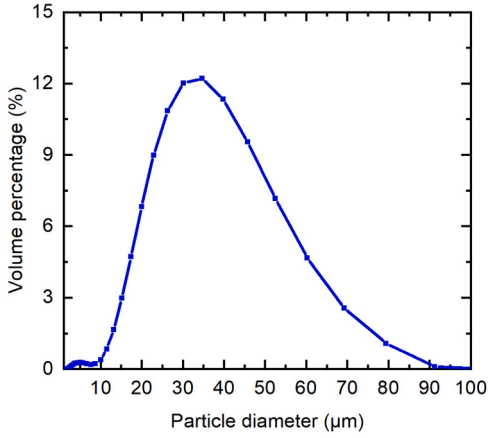

Fig. 1. Particle size distribution of Ti-6Al-4V feedstock powder.

build plate was heated to 100 °C. A carbon fibre blade provided by EOS was used for recoating powder. The laser beam has a D4σ of 80 μm under a laser power of 200 W. A nominal laser beam diameter of 100 μm was applied on the EOS build preparation software. The F-theta lens has a working distance (from the front optic to the workpiece) of approximately 500 mm.

The specimens were built with a laser power of 280 W, scan speed of 1200 mm/s hatch distance of 0.14 mm and layer thickness of 30 μm. A striped scan pattern was used, with stripe width of 10 mm. The scan orientation was rotated 67° between deposition layers. According to the EOS default setting, the contour of the scanned area is usually scanned by the laser before and/or after the exposure of the core area of all parts

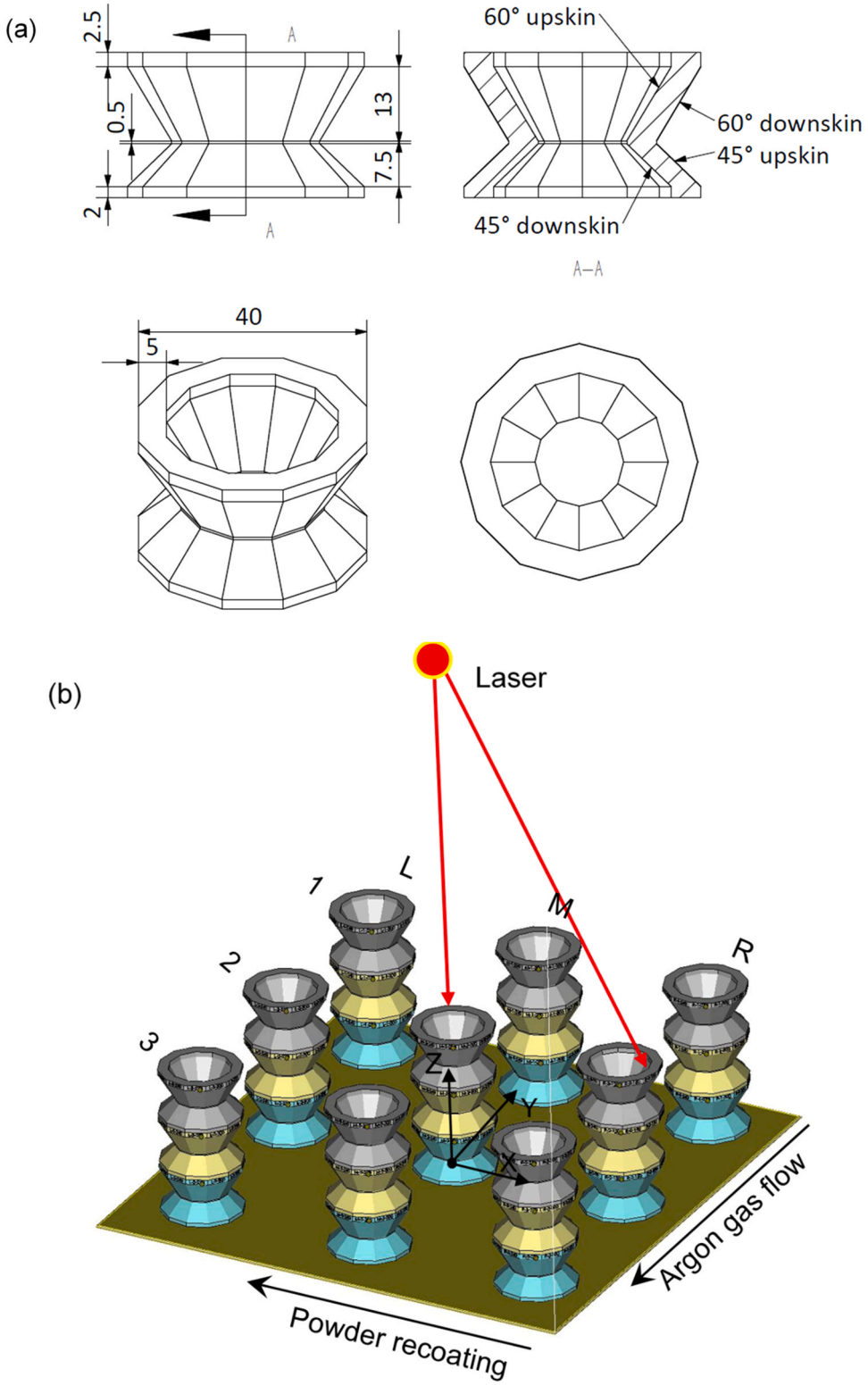

Fig. 2. (a) Pyramid specimen design, four types of inclined surfaces are marked in section view A-A; (b) Arrangement of specimens on an EOS M280 process platform. (For interpretation of the references to colour in this figure legend, the reader is referred to the web version of this article.)

to improve the surface finish. Since the experiment was designed to investigate the influence of exposure sequence on surface roughness, the contour scans were deliberately deactivated to avoid complication of the exposure sequence.

2.3. Specimen design

The design of specimen resembles a pyramid (Fig. 2a) and is a modified version of an earlier design [32]. Each specimen contains 48 individual facets for surface roughness evaluation. The 48 facets can be divided into four groups of 12 facets depending on the orientation relationship between the facet and the horizontal plane, i.e., the build plate. The 12 facets possess 12 discrete orientation angles to the X-axis (recoating direction). The angle between the X axis and the projection of the surface normal vector on the X-Y plane is denoted as α angle. For each of the nine specimen locations, α varies from 20° to 350° in equal steps.

The acute angle between the inclined surface and the build plate is denoted as θ. The angle θ is 60° for the facets in the upper half of the specimen and is 45° for the facets in the lower half of the specimen. For each θ angle, a pair of an upward-facing surface (upskin) and a downward-facing surface (downskin) is obtained. The four groups of testing facets included in a single pyramid specimen are named as 60° upskin, 60° downskin, 45° upskin, and 45° downskin.

2.4. Arrangement of specimen and exposure order

A Cartesian coordinate system is defined with the origin located at the centre of the build area (Fig. 2b). This coincides with the vertical projection of laser origin on the build plate. The recoating and gas flow direction in the EOS M280 are perpendicular to each other. The powder recoating direction is parallel to the X-axis while the gas flow is parallel to Y-axis. The build direction is the Z-axis.

As shown in Fig. 2b, the specimens were placed at nine locations on the build plate, featuring a three-by-three matrix. The projections of the centres of M-2 specimens coincide with the centre of the build plate. The distances between the centres of neighbouring pyramid specimens are 90 mm in both X and Y directions. Each facet in the pyramid thus represents a unique orientation relationship with the laser beam, the gas flow and the recoating direction. At a given location on the build plate, three replicates of the specimen are stacked to form three layers (indicated by different colours). The specimens are labelled according to their positions in the build chamber, i.e., Column (left (L), middle (M) or right (R)) - Row (1, 2 or 3) - Layer of stack (bottom (B), middle (M) or top (T)).

The three layers of pyramid samples were built with controlled exposure sequence of specimens with respect to the gas flow direction, namely: in the same direction as the gas flow for the bottom layer; shuffled for the middle layer; and against the gas flow for the top layer. The specific exposure sequence is shown in Table 1 identified by Roman numerals.

Table 1
Exposure orders designed for three layers of pyramid samples located at different positions. The exposure order is indicated by Roman numerals.

Specimen location (Column-Row)	Exposure order		
	Along gas flow (Bottom layer)	Randomised (Middle layer)	Against gas flow (Top layer)
L-1	I	II	III
L-2	II	VII	II
L-3	III	IX	I
M-1	IV	VIII	VI
M-2	V	III	V
M-3	VI	VI	IV
R-1	VII	V	IX
R-2	VIII	IV	VIII
R-3	IX	I	VII

2.5. Surface profile measurement

The roughness of as-produced specimens was evaluated by tactile profilometry method using a Mitutoyo Surftest SJ 410 (Fig. 3). During measurements, the stylus was set to traverse perpendicular to the layer boundaries. The stylus measurement returns the surface height profile Z (x) at any given position x over an evaluation length of $l = 8$ mm. Five repeating measurements were taken from each facet. A short cut-off length of $\lambda_s = 25$ μm and a long cut-off length of $\lambda_c = 8$ mm were chosen according to the user manual of the surface profilometer. A Gaussian filter was applied to the assessed profile. The stylus used has a tip radius of 2 μm.

2.6. Surface texture parameters

The arithmetical mean of absolute coordinate values Ra was recorded manually while measuring surface roughness using profilometer. The surface roughness profiles were saved and then exported to MATLAB software for further analysis. Several surface texture parameters were then computed according to ISO 4287:1997 [35]. In addition to Ra values, described by Eq. (1), five additional surface roughness parameters are presented. The root mean squared deviation of assessed profile Rq (Eq. (2)) was used as an additional amplitude parameter. The root mean square of local slope RΔq (Eq. (3)) was used to assess how abruptly the surface height changes locally, while the local slope dZ/dx is estimated using Eq. (4) for discrete measurement points. The mean width of profile element R_{sm} (Eq. (5)) is a parameter for horizontal spacing between peaks and valleys. A profile element consists of a surface profile peak and its adjacent valley. A height discrimination (10% Rz) and a spacing discrimination (10% sampling length) were applied when identifying the peaks and valleys of surface profile as suggested by ISO 4287:1997 [35]. Rsk (Eq. (6)) and Rku (Eq. (7)) are used as measures of the asymmetry and sharpness of probability density function of surface height values [35].

$$Ra = \frac{1}{l}\int_0^l |Z(x)|dx \tag{1}$$

$$Rq = \sqrt{\frac{1}{l}\int_0^l Z^2(x)dx} \tag{2}$$

$$R\Delta q = \sqrt{\frac{1}{l}\int_0^l \left[\frac{dZ(x)}{dx}\right]^2 dx} \tag{3}$$

$$\frac{dZ_i}{dx} = \frac{1}{60\ \Delta X}(Z_{i+3} - 9Z_{i+2} + 45Z_{i+1} - 45Z_{i-1} + 9Z_{i-2} - Z_{i-3}) \tag{4}$$

$$Rsm = \frac{1}{m}\sum_{i=1}^{m} Xs_i \tag{5}$$

$$Rsk = \frac{1}{Rq^3}\left[\frac{1}{l}\int_0^l z^3(x)dx\right] \tag{6}$$

$$Rku = \frac{1}{Rq^4}\left[\frac{1}{l}\int_0^l z^4(x)dx\right] \tag{7}$$

2.7. Electron microscopy

Scanning Electron Microscopy (SEM) images were taken from selected facets for qualitative comparison between facets of different orientations using a FEI Quanta 3D FEGSEM electron microscope in

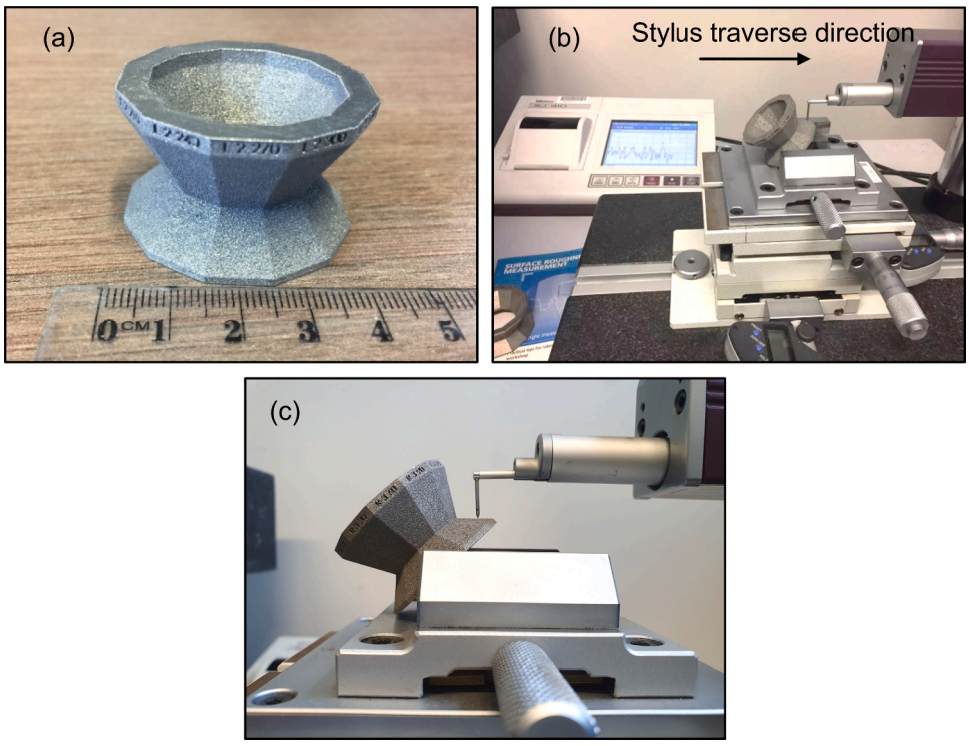

Fig. 3. Pictures of (a) a pyramid sample removed from build plate, (b) a specimen mounted on the Mitutoyo Surftest SJ410 surface profilometer, the facet being tested is 45° upskin surface. (c) the measurement stylus in contact with specimen surface, the stylus is perpendicular to the tested facet.

Secondary Electron Imaging (SEI) mode. The specimen surface was rotated to horizontal position when images were taken.

2.8. Neural network model

2.8.1. Definition of input variables

Since each facet in a pyramid specimen represents a unique geometrical relationship with the machine, seven input parameters were calculated to define the orientation and location of each facets. In addition, the exposure order of a given specimen along the gas flow direction was indicated by a number N. Hence, there are eight input parameters in total to describe each facet in the pyramid experiment, i.e. the input layer has eight neurons, as shown in Table 2.

A build-up orientation with the maximum expected Ra value was defined (Fig. 4) based on previous studies [32–34] and the observations in the current work. This orientation changes as the specimen's location on the build plate changes. It is hypothesised that any deviation from this build-up orientation would result in a reduction in Ra values at any location on the build plate. Hence, the angular displacement δ angle as defined in Fig. 3 was chosen as one input variable for neural network training.

Table 2
Description of input parameters for neural network training.

Input variable	Description
θ	Surface orientation angle to the build plate
ud	Upskin (coded 1) or Downskin (coded −1)
X	X coordinate with origin at the centre of the build plate
Y	Y coordinate with origin at the centre of the build plate
Z	Vertical distance from the middle of the facets to the build plate
R	Radial distance between the middle of the facet and the centre of the build
δ	Angular displacement from the build-up orientation with maximum expected roughness
N	Exposure order of sample in its column

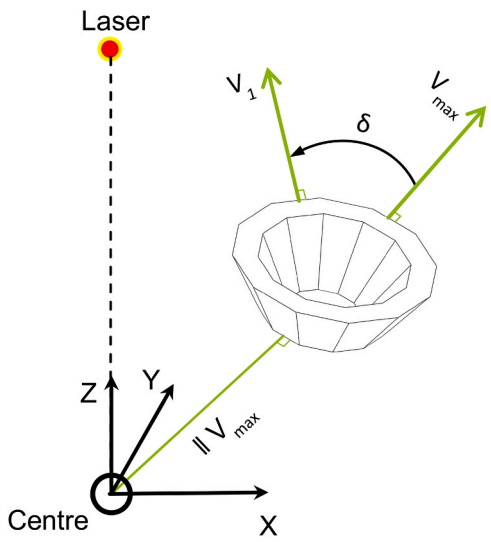

Fig. 4. Schematic illustration of build-up orientation of inclined surfaces (upskin and downskin) with maximum expected Ra values. The part drawing represents the upper half of a pyramid specimen. V_1 and V_{max} are two vectors that are parallel to the build plate (X-Y plane), V_{max} indicates the build-up orientation of an inclined surface with maximum expected Ra. δ angle is the angular displacement from V_{max} to V_1 in the anticlockwise direction. V_1 and V_{max} are perpendicular to the respective specimen edges.

2.8.2. Training

The neural network model was constructed using the built-in "neural fitting" tool in Deep Learning Toolbox 13.0 of MATLAB software. A Bayesian regularisation method was chosen as the training algorithm.

The Ra values measured from the facets of the pyramid specimens were used as the target layer. One hidden layer of 12 neurons were used for neural network training.

The training dataset consists of an input matrix with a dimension of 1296 observations of eight elements and a target layer with a dimension of 1296 observations of one element (Ra value). The data was divided into three parts as follows: training 70%, validation 15%, and test 15%. The validation dataset was used as a feedback to the training process to improve the accuracy of prediction, while the test dataset was used to evaluate independently how well the regression model predicts results that are not included in the training process.

2.8.3. Application of neural network model

The trained neural network model was used to run virtual experiments to evaluate the variation in output (Ra values) in response to the changes in inputs (orientation, location, exposure sequence). An area on the build plate with a dimension of 180 mm × 180 mm were meshed to give 30 × 30 coordinate points on the X-Y plane defined in Fig. 2. The investigated area is centred around the centre of the build platform. The coordinate values are then used as two of the input variables for neural network prediction. Other input variables as defined by Table 2 were arbitrarily varied to investigate their effects on surface roughness.

3. Results

3.1. Ra value variation across the build volume

The measured Ra values are summarised in Table 3 for the four different surface orientations to the build plate. The Ra values of 60° upskin surfaces possess a mean of 26.6 μm, the largest standard deviation of 5.5 μm and a range from 17.6 μm to 43.4 μm. The Ra values of 45° upskin surfaces have a similar mean, and slightly lower standard deviation and narrower range. The 45° downskin surfaces show the highest mean Ra value of 28.9 μm, slightly narrower deviation and range compared to the upskin surfaces. The Ra values of 60° downskin surfaces show the lowest mean, deviation and range.

The Ra values measured from the individual facets are plotted in Fig. 5 to Fig. 8 with three series of data acquired from stacked specimens at the given locations. The variation in Ra values has a clear dependency on α angles in all pyramid specimens apart from M-2 specimens that are located directly under the laser. This observation leads to the conclusion that the variation in Ra values originates partly from the orientation of the facets to the laser. The specimens at locations other than the centre (M-2) were irradiated by the laser beam with a wide range of incidence angles. In each of the pyramid specimens not located at the centre directly under the laser origin, the orientation relationship between the individual facets and the laser changes with sample location and α angle. By contrast, the laser incidence angle to the facets in M-2 specimens remain constant for the 12 facets of various α angles at given orientations to the horizontal plane.

In Fig. 5, the 60° upskin surfaces in L-1 specimens with α angles in the range of 50–200° show higher Ra values than the other half. At the opposite corner in R-3 specimens, the facets with α angles of 20° and in the range of 230–350° show higher Ra values than the rest, which is exactly the opposite to what was found in L-1 specimens. This holds true for the pairs of specimens located at opposite sides and corners of the build platform, namely, M-1 and M-3, R-1 and L-3, L-2 and R-2. The Ra values of 60° downskin surfaces (Fig. 6) span across a narrower range but follow a patten of variation similar to that of 60° upskin surfaces (Fig. 5). It is noteworthy that the patterns in which the Ra value varies with α angles for 45° upskin (Fig. 7) and 45° downskin (Fig. 8) are similar to each other but different from 60° upskin and 60° downskin. This difference originates from the different build-up orientation of the facets to the centre of each specimen, and thus the orientations to the laser of the facets at given α angles are different. One needs to refer to the specimen design and arrangement over the build area in Fig. 2 for this analysis. The facets in the upper half of each pyramid specimen (60° upskin and 60° downskin) were built up and *outwards* from the centre of the specimen, thus the facets located at the outer perimeter of the build platform were built up and *away* from the laser. On the contrary, the facets in the lower half of each pyramid specimen (45° upskin and 45° downskin) were built up *inwards*, hence the facets at the outer perimeter of the build platform were built up and *towards* the laser.

Considering the specimen design and arrangement, it is then possible to generalise a description of the pattern in which the Ra values vary - with given orientation to the horizontal plane, the facets built up and *towards* the laser have lower Ra values than those built up and *away* from the laser.

Table 3
Descriptive statistics of measured Ra values. All the values are in the unit of μm.

	60° upskin	60° downskin	45° upskin	45° downskin
Mean	26.6	20.7	26.6	28.9
Standard deviation	5.5	3.2	5.2	4.6
Minimum	17.6	13.7	16.5	19.1
Maximum	43.4	29.7	42.5	42.2
Range	25.8	16.0	26.0	23.1

3.2. Surface texture

The product surface texture is highly complex and shows variation with different α angles (Fig. 9). At all α angles similar features are seen. Distinct powder particles of varying size, cavities, and aggregates of partially melted powder particles are present. The rougher facets in a pyramid specimen (Fig. 9c–e) exhibit large aggregates of partially melted powder particles and cavities. The smoother facets in Fig. 9a, b and f show surfaces of fewer aggregates and shallower cavities, while partially melted particles are evenly dispersed over the surface.

The change in surface texture with varying α angles lead to differences in the surface profiles measured by tactile profilometry and resultant surface texture parameters (Fig. 10). Within the range of α angles from 140° to 290° of L-3-B specimen the roughness profiles possess wider distributions of ordinate values (Fig. 10a) and occurrences of isolated, large peaks and valleys (Fig. 10b). As the build-up orientation of the inclined surfaces changes from “towards the laser” (α = 50°) to “away from the laser” (α = 230°), the respective changes in surface texture parameters (Fig. 10c) indicate that the roughness profile gradually changes towards larger mean peak/valley amplitude (higher Ra and Rq), steeper local slope (higher RΔq), wider peaks and valleys (higher Rsm), less positively skewed surface (lower Rsk value) and less frequent change between peaks and valleys (lower Rku values). This change in surface texture with differing build-up orientations to the laser is found in all specimens not located at the centre.

3.3. Comparison among groups

As concluded in Section 3.1, the surface’s orientation to the laser plays a major role in the roughness values. However, it is not the sole factor determining the roughness of inclined surfaces, if otherwise the Ra values measured would have been symmetric with respect to the centre of the build and there would be no significant difference among the three layers of the stacked pyramid specimens.

The box plots in Fig. 11 compare the frequency distributions of Ra values measured at various positions in the build chamber. The range of Ra data distribution seen in each box plot indicate the variation in surface roughness at the location where the specimen was fabricated.

For upskin surfaces, the Ra values exhibit the narrowest range in M-2 specimen among the nine locations. For 45° downskin surfaces, R-2 and R-3 specimens show similar spreads in Ra data compared to M-2 specimen, while others show larger spreads. For 60° downskin surfaces, the overall variation in Ra values is not as pronounced as for the other surface orientations, and slightly less variations are found for the specimens made in the right column close to the powder feedstock.

At a given position on the build plate, there are differences in Ra

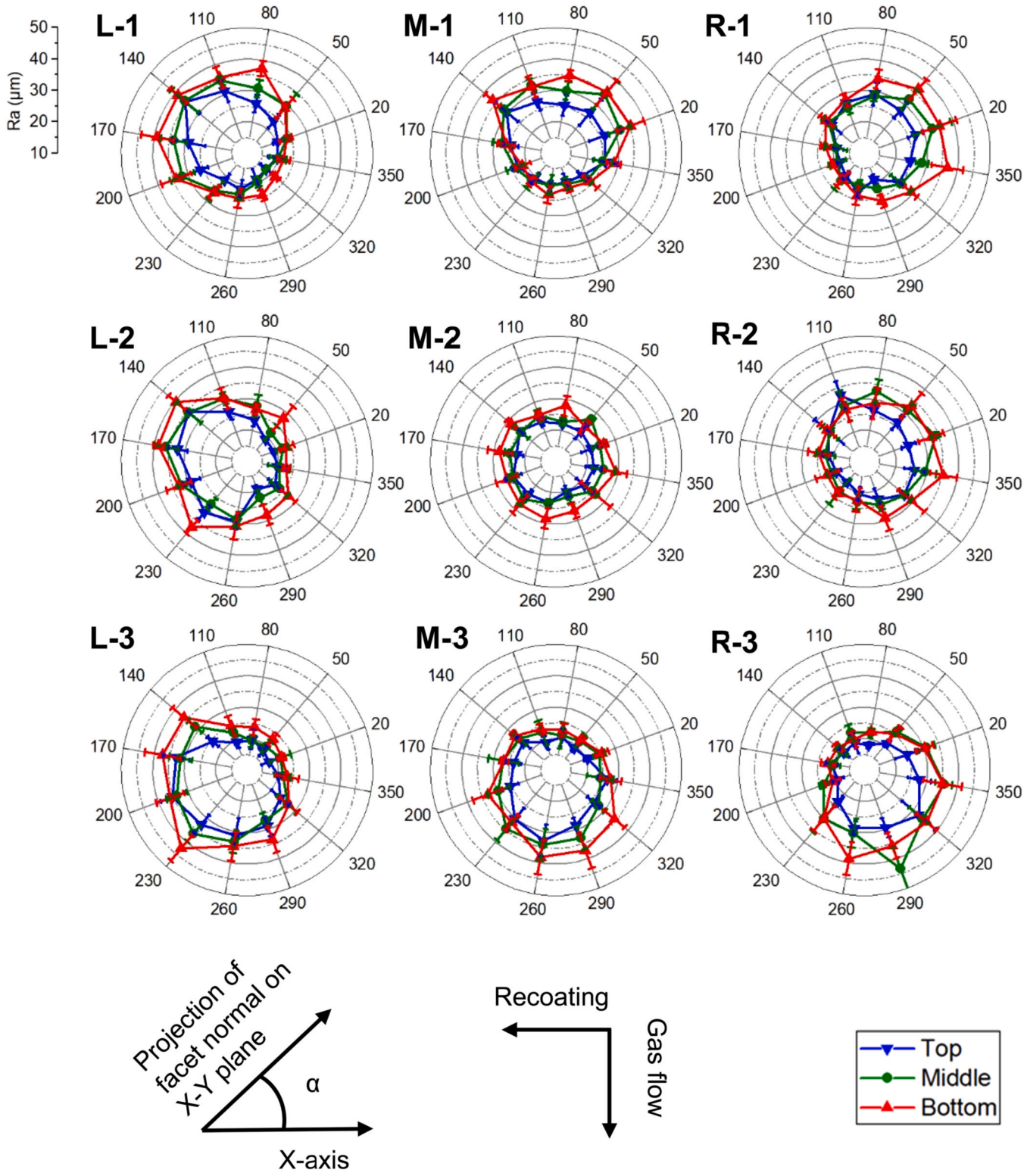

Fig. 5. Plots of Ra values of 60° upskin surfaces, each polar graph includes data measured from three stacked specimens built at a certain location on the build plate. The angular position α of each facet is defined by the angle between the projection of facet surface normal and the X-axis.

values among the three stacked pyramid specimens. The exposure sequence as designed (Table 1) is expected to influence the surface roughness by modulating the effects of process by-products such as smoke and spatter. The heat extraction from the melt pool becomes slower as the build height increases constantly from the bottom to the top layer, which can also affect roughness [20]. However, these two factors are convoluted in the current study and it is not straightforward to draw conclusions about which factor overpowers the other. For 60° upskin surfaces, there are clear separations in the Ra values among the three stacked layers across the entire build, especially for the facets that were built up and away from the centre of the build (Fig. 5). The overall Ra data show an increase in median values and the width of distribution

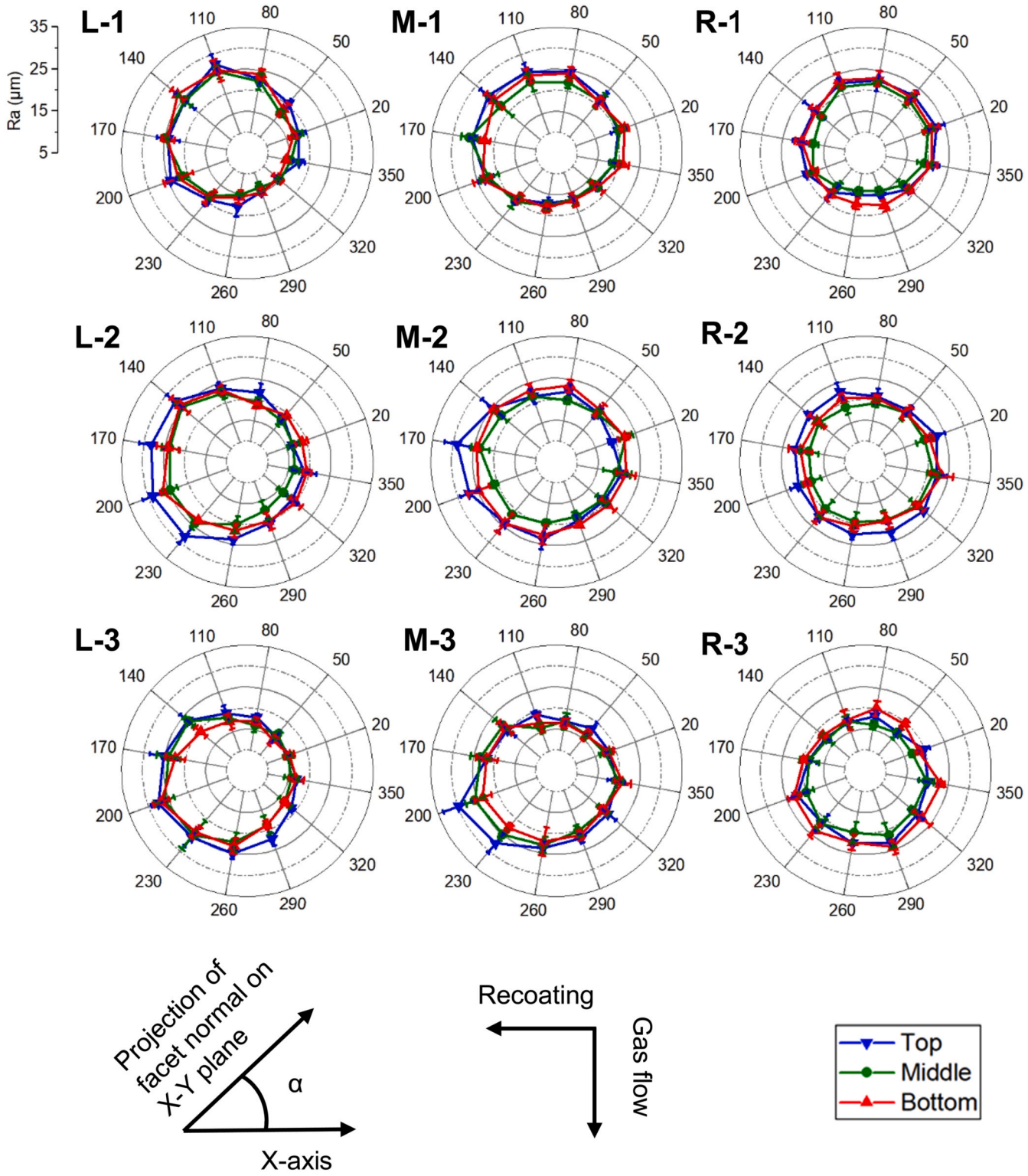

Fig. 6. Plots of Ra values of 60° downskin surfaces, each polar graph includes data measured from three stacked specimens built at a certain location on the build plate. The angular position α of each facet is defined by the angle between the projection of facet surface normal and the X-axis.

from the top layer to the middle and bottom layers of stack (Fig. 11). Combining the observations from Fig. 5 and Fig. 11, the three layers of specimens show an increased dependency on build-up orientation (α angle) from the top layer to the middle and bottom layers. For 45° upskin surfaces, the roughness value does not change monotonically with the changing layer of stack (Fig. 11), which is also clear based on the individual observations in Fig. 7. The downskin surfaces generally do not show as steep variation in Ra values with different layer of stack as the upskin surfaces do. In most cases for 45° downskin and 60° downskin surface with only a few exceptions, the first quartile of Ra data is the lowest for the middle layer of stack.

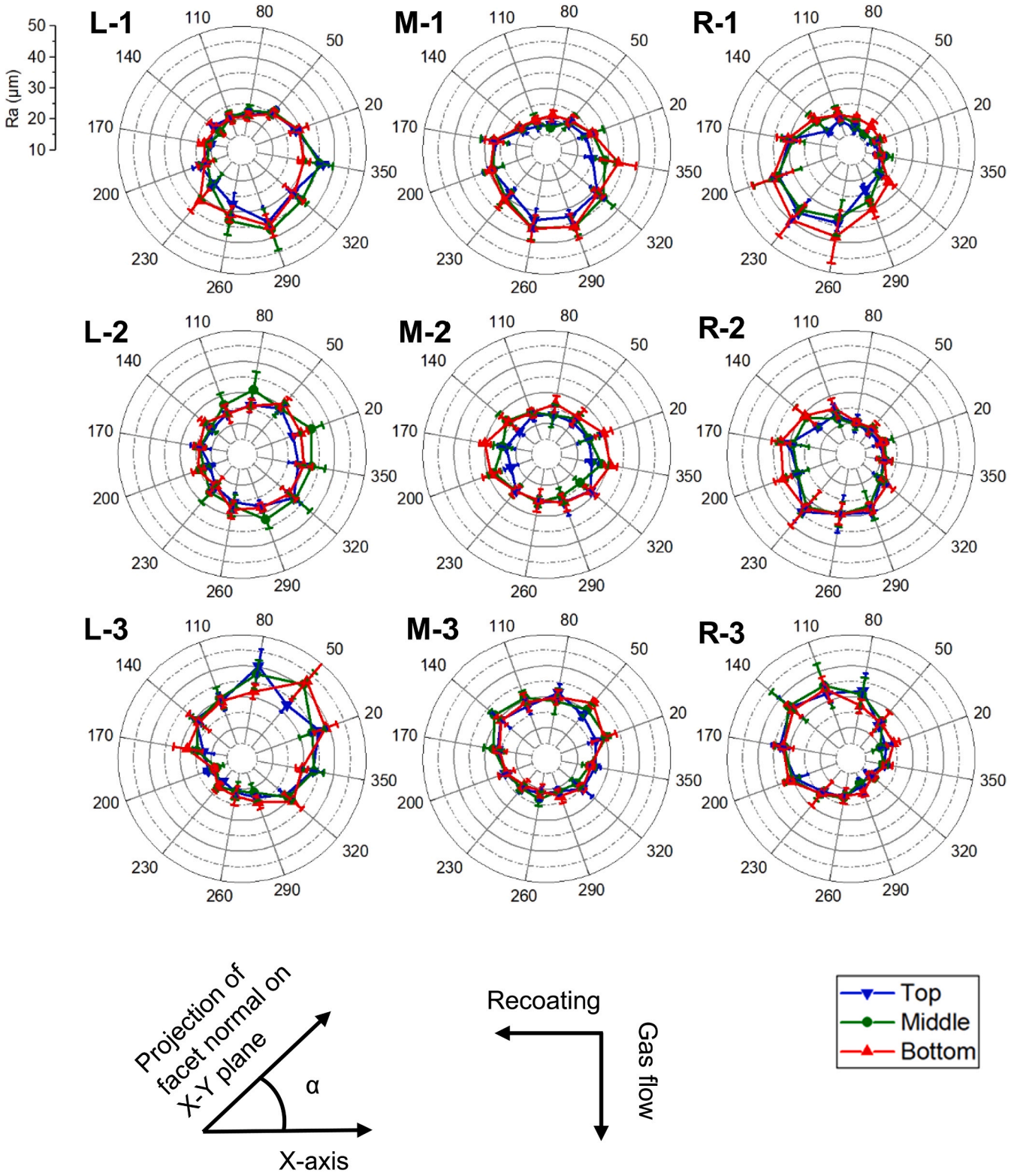

Fig. 7. Plots of Ra values of 45° upskin surfaces, each polar graph includes data measured from three stacked specimens built at a certain location on the build plate. The angular position α of each facet is defined by the angle between the projection of facet surface normal and the X-axis.

3.4. Neural network model for variation in surface roughness

The regression R values indicate the percentage of variance in the experimental data that is encountered by the neural network models. R values of 94% for the training dataset and 92% for the test dataset were achieved for the neural network model. During the training process, the test dataset was put aside for testing how the neural network predicts new observations that are not included in the training dataset. The high absolute value of R for the test dataset indicates a good ability of neural network model in predicting the experimental values. The similar values of R for training and test dataset indicate no significant overfitting.

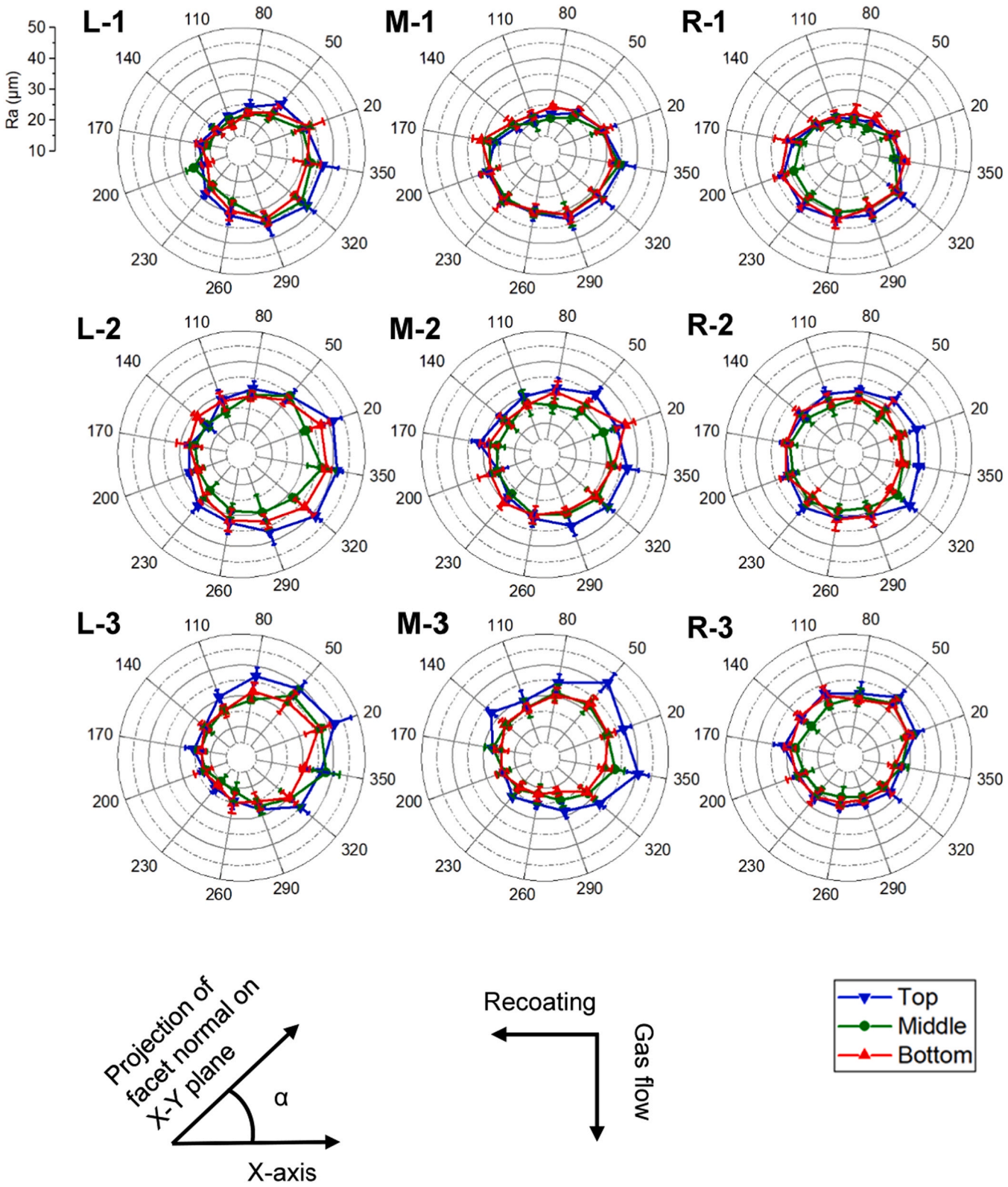

Fig. 8. Plots of Ra values of 45° downskin surfaces, each polar graph includes data measured from three stacked specimens built at a certain location on the build plate. The angular position α of each facet is defined by the angle between the projection of facet surface normal and the X-axis.

3.4.1. Sensitivity analysis using neural network model

It is clear from the experimental data that the build-up orientation (δ angle as defined in Fig. 4) of the inclined surfaces has a prominent effect, but it is not clear how build height or changed exposure sequence contribute to the difference in roughness among specimens stacked at the same locations (Fig. 11). The neural network model can be used to run virtual experiments to rationalise the influence of individual factors on surface roughness. One can evaluate the effects of individual factors by examining the change in Ra values predicted by the neural network model in response to an arbitrary amount of change to the input

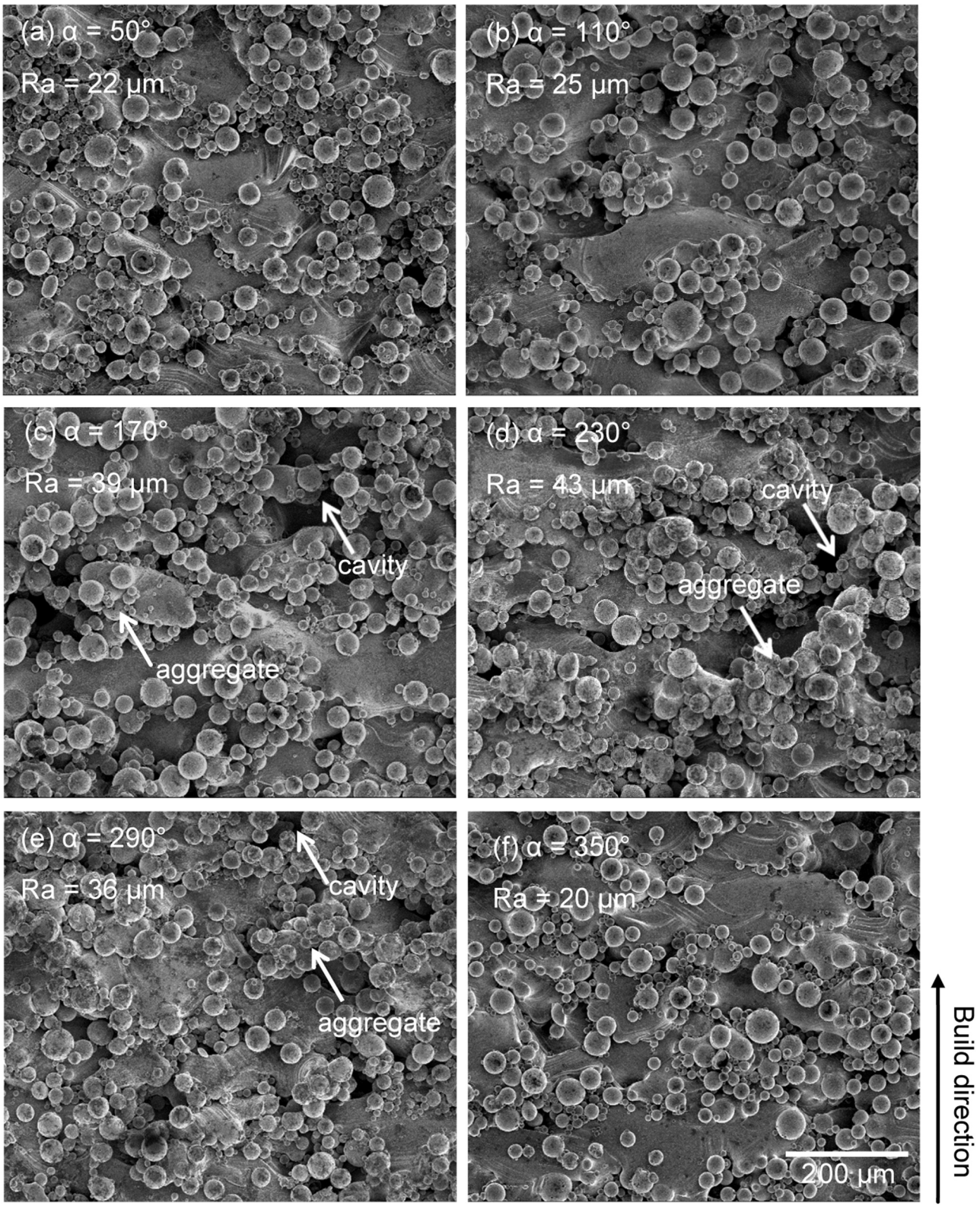

Fig. 9. SEM images of selected facets in specimen L-3-B on 60° upskin surfaces (located at left column, third row and bottom layer of the stacks). Corresponding surface profiles and surface texture parameters are presented in Fig. 10.

variables.

Fig. 12 and Fig. 13 are contour plots of the predicted Ra values for 60° upskin and 45° downskin respectively across a build area of 180 mm × 180 mm in an EOS M280 machine, with the centre of the build plate coinciding with the centre of the plotted area. The prediction of the neural network is restricted to the window of conditions covered by the experiments and its accuracy is validated by the high R value from the test dataset.

In both Fig. 12 and Fig. 13, (a) is used as a baseline for comparison with (b), (c) and (d) for the effects of build height, exposure sequence

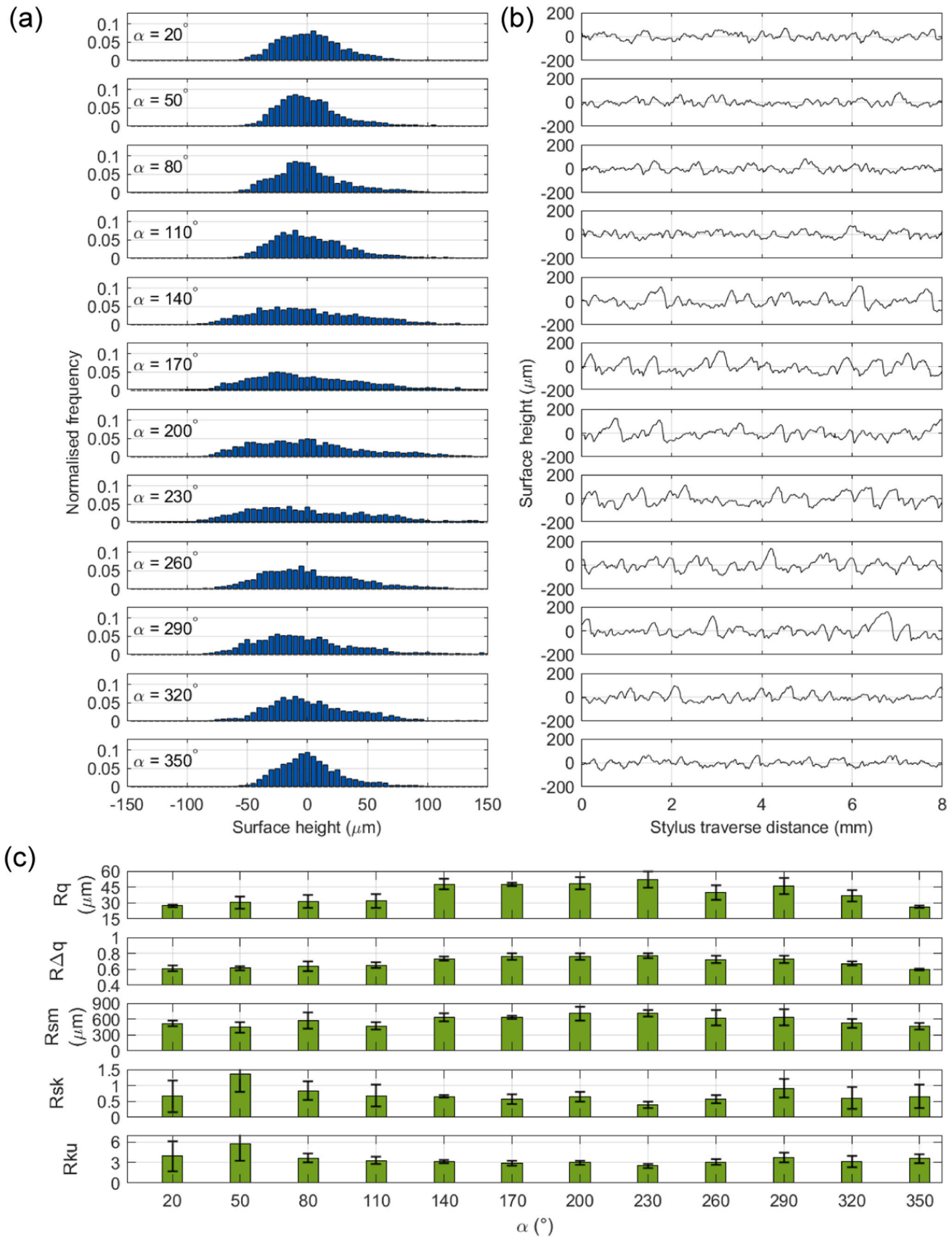

Fig. 10. (a) Surface height distribution, (b) roughness profile and (c) the corresponding surface texture parameters measured from 60° upskin surfaces of specimen L-3-B.

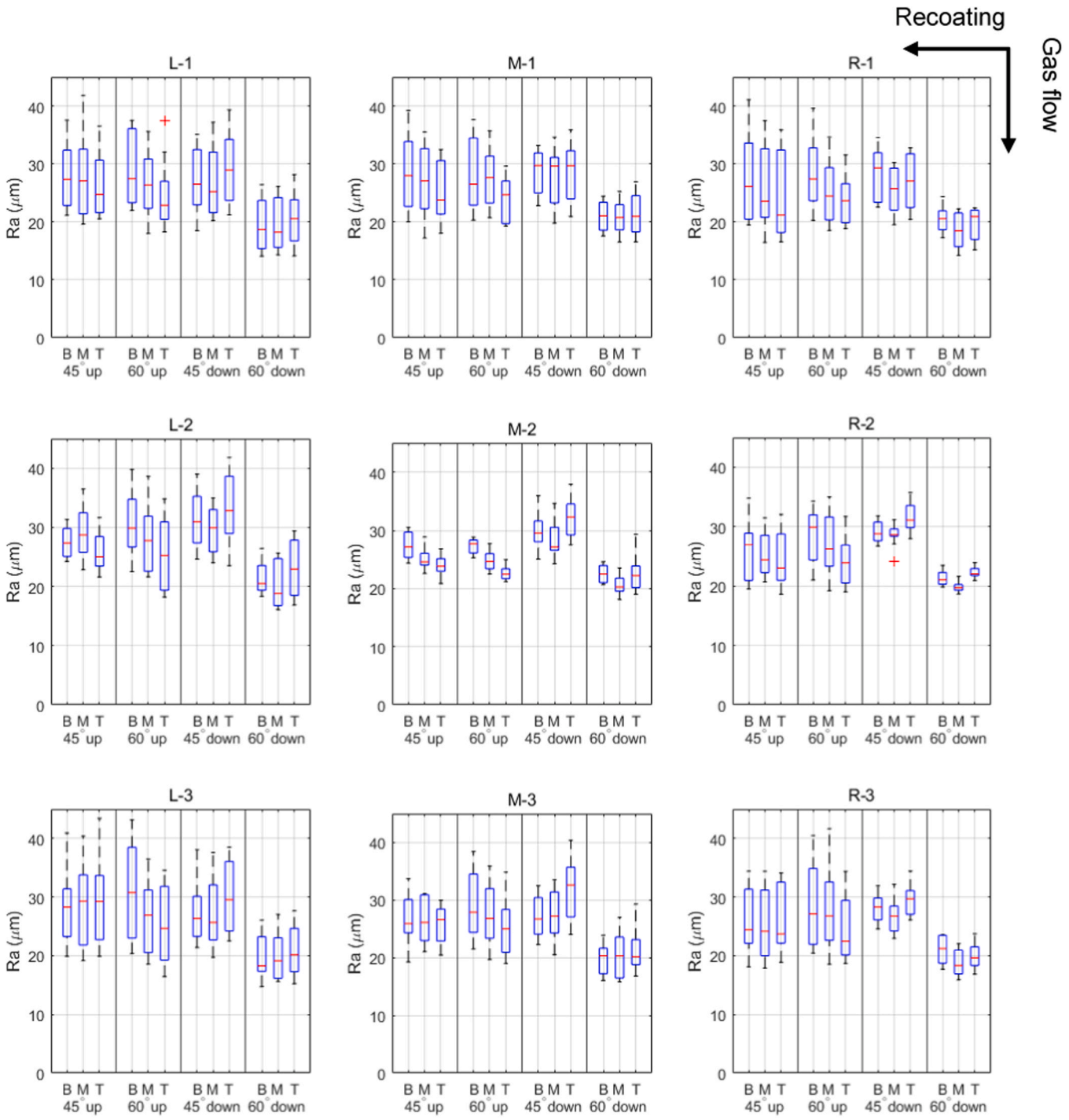

Fig. 11. Box plots of Ra values measured from the pyramid specimens at nine discrete locations on the build plate. The groups are labelled as B, M, T (bottom, middle, top layer of the stacked pyramid specimens) and 45° up (upskin), 60° up, 45° down (downskin) and 60° down. The bottom and top edges of the boxes indicate the first quartile (Q1) and the third quartile (Q2) of the data. Ra values greater than Q3 + 1.5 (Q3 - Q1) or smaller than Q1 - 1.5 (Q3 - Q1) are considered as outliers (marked by red cross). The whiskers extend to the highest and lowest observation that are not considered outliers. (For interpretation of the references to colour in this figure legend, the reader is referred to the web version of this article.)

and build-up orientation (δ angle). As one compare Fig. 12a and b, the change in build height from 20 mm to 70 mm generates lower Ra value across the entire build plate for 60° upskin surfaces. However, for the case of 45° downskin, the same change in build height result in higher overall Ra values across the build, as shown by Fig. 13a and b. The role of exposure sequence is not as clear as one compares (a) with (c) in Fig. 12 or Fig. 13. Finally, the comparisons between (a) and (d) in Fig. 12 and Fig. 13 show the dominant effect of build-up orientation (δ angle) on the roughness value and its variation. As the inclined surfaced are built up and towards the centre ($\delta = 180°$ shown in Fig. 12d and Fig. 13d), Ra value is relatively low and shows good consistency over the build area. In the case where $\delta = 0°$, the inclined surfaces are built up and away from the centre, the Ra value across the build increases in magnitude and spread (shown in Fig. 12a and Fig. 13a).

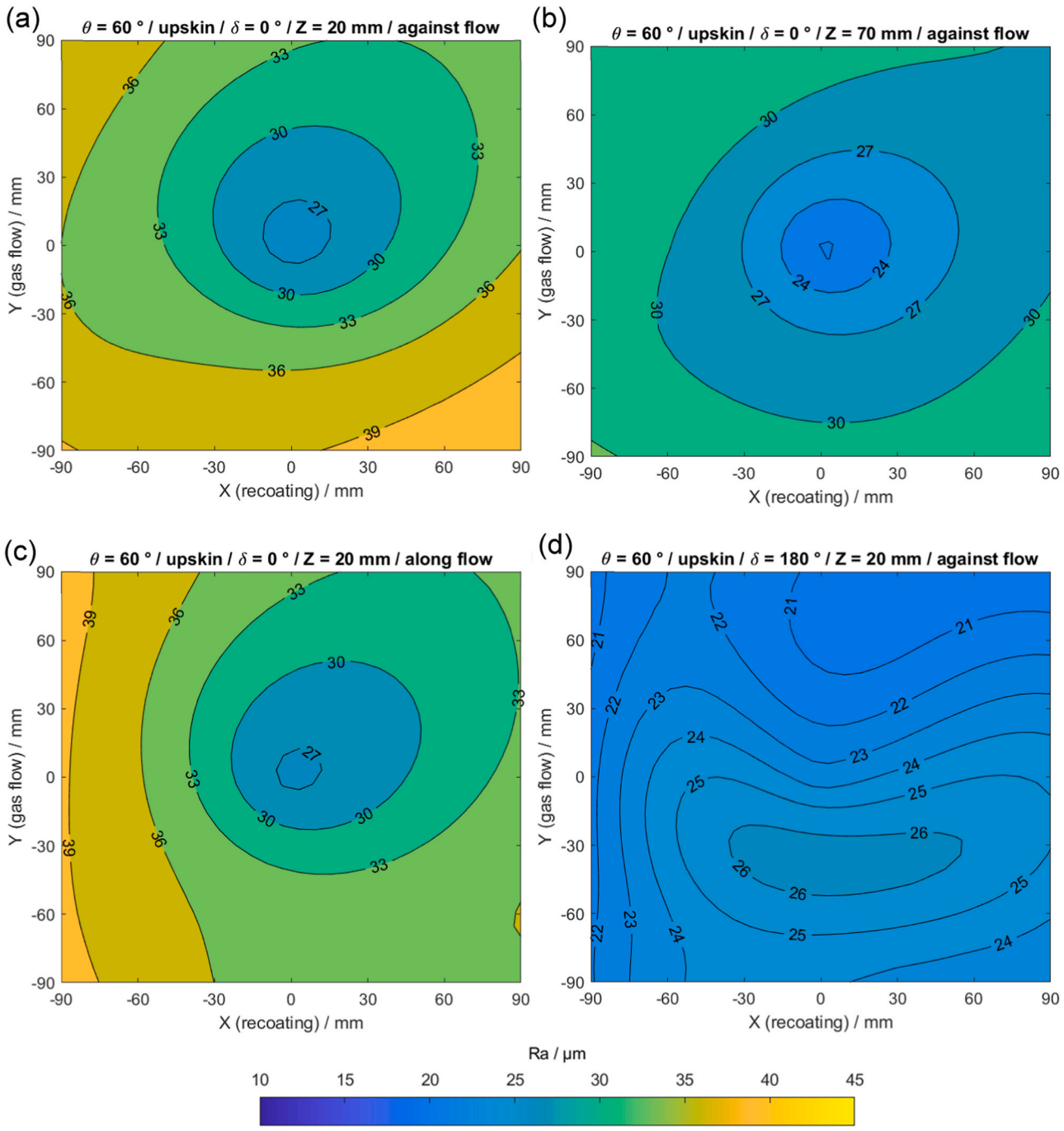

Fig. 12. Conotur plots of surface roughness (Ra) variation predicted by neural network model across the build for 60° upskin surfaces of LPBF Ti-6Al-4V alloy products built in EOS M280 machine.

3.4.2. Heat maps of mean value and variance

Heat maps in Fig. 14 and Fig. 15 show the change of Ra predicted by neural network model with differing build height and build-up orientation (δ angle) in terms of mean value and variance. Each of the mean and variance values was calculated from a 30 × 30 Ra value matrix predicted by neural network model over a meshed build area of 180 mm × 180 mm as described in Section 2.8.3.

For 60° upskin surfaces (Fig. 14), the mean value of Ra appears lowest for relatively large build height and δ angle in the vicinity of 180°. The highest mean values of Ra appear at bottom of the build (5–10 mm from the base plate) and δ angle close to 0°, noting that δ angles in the range of 300–330° are effectively close to δ = 0° (equivalent to 360°). The variance of Ra over the estimated build area generally has a similar trend as the mean value, i.e. higher variance where mean value is higher. It is noteworthy that both the mean and variance of Ra decrease monotonically with increasing build height, regardless of the build-up orientation.

In the case of 45° downskin surfaces, there is a window of build height (20–45 mm) and δ angle (90–210°) where the Ra mean values are relatively low (25–27 μm) as is shown in the middle part of Fig. 15a. Unlike the case in 60° upskin (Fig. 14a), the Ra mean value of 45° downskin is relatively high at both ends of the spectrum of build height (Fig. 15a). The change in Ra mean value over the build in 45° downskin (Fig. 15a) is not as significant as the 60° upskin (Fig. 14a). However, the variance across the build in Ra value of 45° downskin increases significantly with the build height (Fig. 15b). To view this variance in more

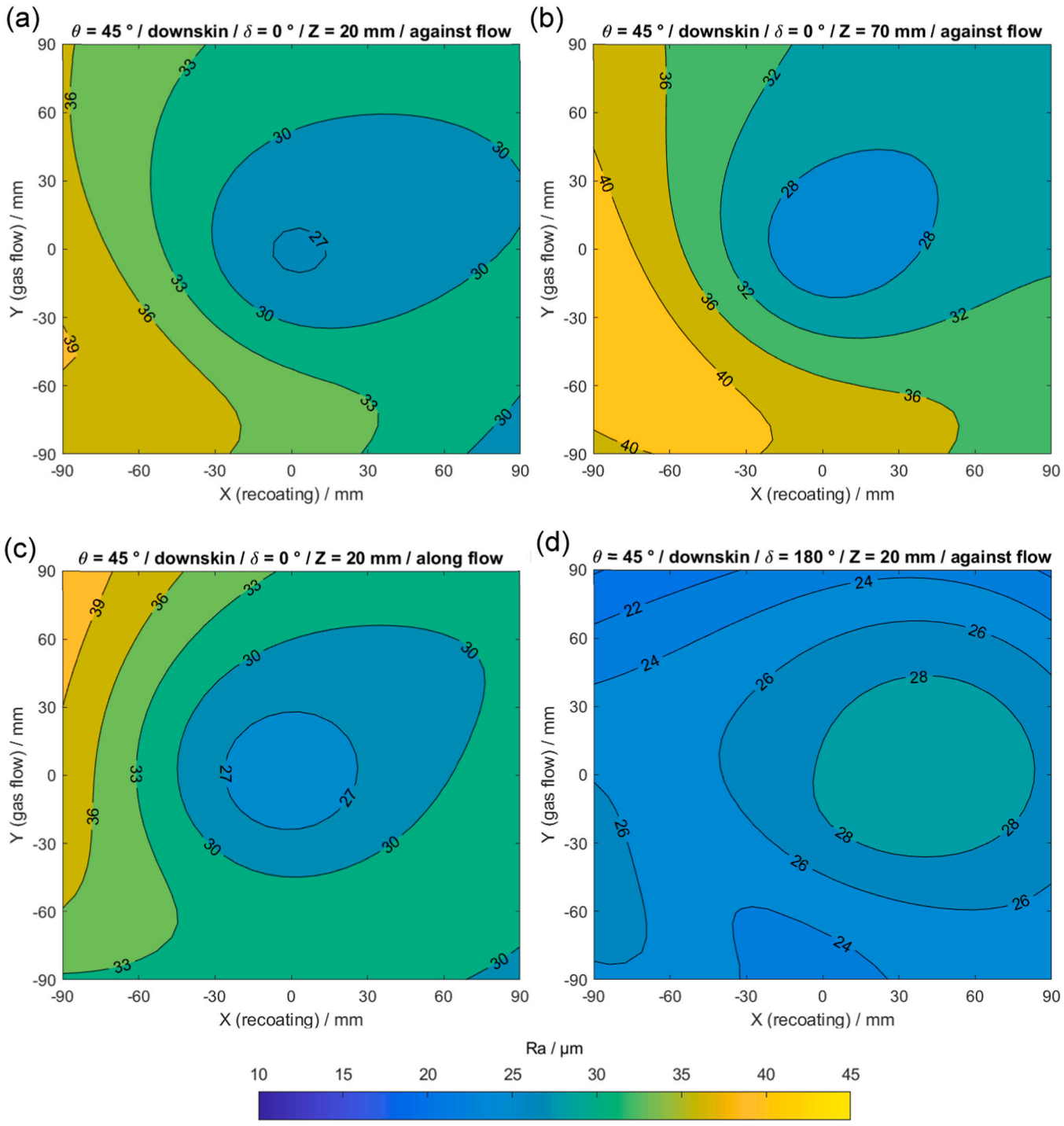

Fig. 13. Conotur plots of surface roughness (Ra) variation predicted by neural network model across the build for 45° downskin surfaces of L-PBF Ti-6Al-4V alloy products built in EOS M280 machine.

detail, the high Ra value region (Ra > 35 μm) from the left bottom corner (close to the powder overflow and gas outlet) expands with increase in build height (Fig. 13a and b).

4. Discussion

4.1. Effects of build-up orientation and distance from the centre

The Ra values measured from our specimens exhibit more variation compared to what is already in literature. One may be surprised that a 60° upskin surface can be rougher than a 60° downskin surface and nearly as rough as a 45° downskin surface (Table 3) based on the notion that downskin surfaces are rougher as they encounter excessive heat input and accumulation and thus exhibit higher roughness because of thermal distortion and melt pool extension [37]. The 60° upskin surfaces in the current study possess higher mean and larger range in Ra values (Table 3) than what is found in most of the studies where Ra values for 60° upskin surfaces are typically in the range of 10–23 μm [30,36,37]. However, direct comparison is not possible because of the variety of machine, material, powder feedstock, geometry of test specimen and processing parameters used. Meanwhile, a large scatter is often present in roughness measurements of L-PBF products [32,34]. It is therefore

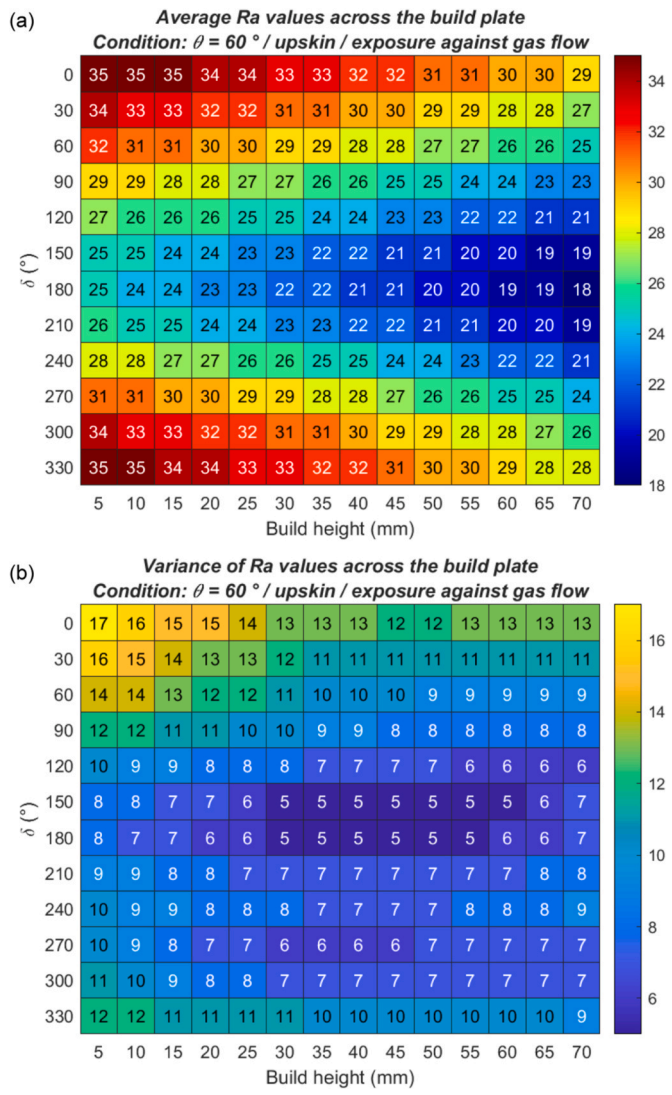

Fig. 14. Heat maps of (a) mean values and (b) variance of Ra values predicted by neural network model for 60° upskin surfaces in EOS M280 machine over a build area of 180 mm × 180 mm centred around the centre of the build platform.

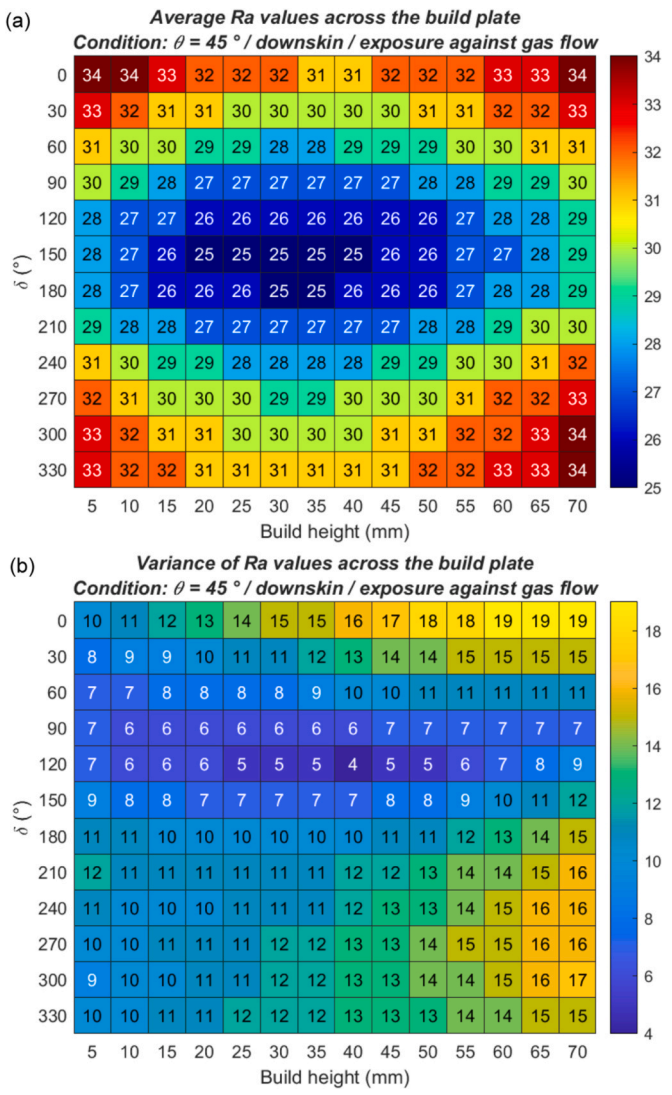

Fig. 15. Heat maps of (a) mean values and (b) variance of Ra values predicted by neural network model for 45° downskin surfaces in EOS M280 machine over a build area of 180 mm × 180 mm centred around the centre of the build platform.

necessary to separate the origins of such scatter in surface roughness in order to explain the trends in the measured data, and the comparison with the literature.

A general trend applicable to all the specimens measured is that Ra value reaches maximum for inclined surfaces at a given corner or edge of the build plate when the inclined surfaces were built up and away from the centre. The build-up orientation effect on surface roughness becomes more pronounced as the specimen locates farther away from the centre of the build. This is in agreement with the result in [32] where similar specimens were built in separate builds on an EOS M270 machine to rule out other effects such as spattering and recoating effect.

In an EOS M280 machine, the laser beam originates from above the centre of the build plate. As the laser beam is directed away from the centre of the build plate, the laser incidence angle β (Fig. 16a) to the powder bed surface deviates from normal angle. As the laser originates from approximately 500 mm (working distance of F-theta optics) above the centre of a 250 mm × 250 mm build platform, yielding a minimum of 74° incidence angle at the very corner of the build plate as opposed to 90° at the exact centre. In addition, the inclined surfaces are built up and toward various directions relative to the centre of the build. This orientation effect is elucidated in the schematic drawings of Fig. 16 that is a further development from the explanation in Ref. [32]. This difference in orientation would incur differences in heat input on surfaces. Here one possible explanation of the problem is provided. In the case of upskin, the laser beam is approximately aligned with the inclined surface in the scenario of surface 1 (Fig. 16b), which promotes the inter-layer wetting through re-melting of previous layers, whereas in the scenario of surface 2 (Fig. 16c) laser points towards the bulk solid and impose less re-melting of previous layers. As a result, orientation like surface 1 tends to produce smoother surface than surface 2. In the case of downskin, the laser is again more aligned with the inclined surface in the scenario of surface 3 and thus benefit the inter-layer wetting. Whilst downskin surfaces are generally expected to be rougher than upskin surfaces due to the melt pool extension into the powder bed as a result of lack of heat conduction during laser melting process, the angle of the surface to the build plate, θ, and the layer thickness also come into play. More importantly, the laser points towards the powder bed in the scenario of surface 4, which exacerbates the melt pool extension on downskin. Consequently, surface 3 should be smoother than surface 4. Meanwhile, the ejection trajectories of spatter and entrained particles possess certain relationship with the scan direction [8,18]. The direction of particle ejection and laser beam attenuation at the edge of the scan

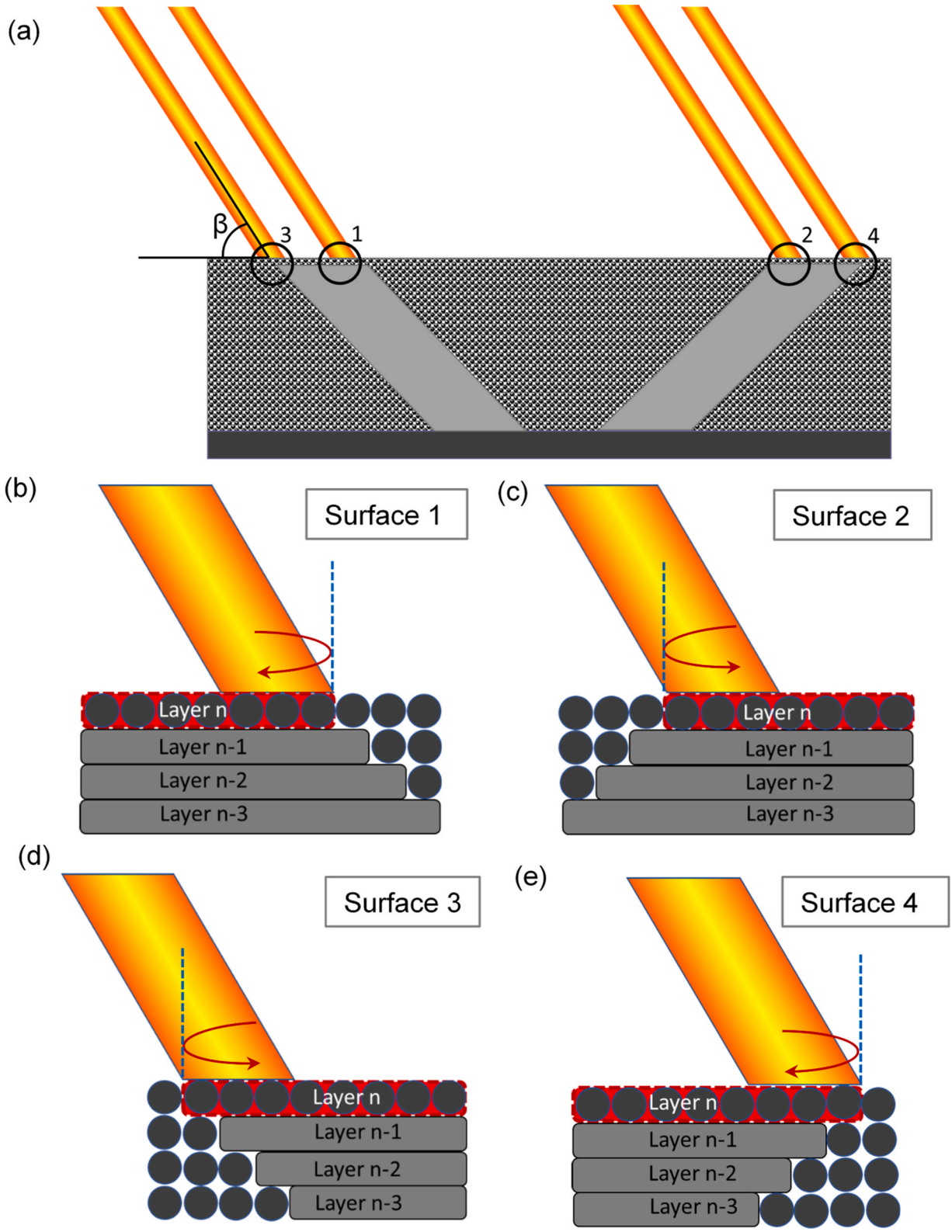

Fig. 16. Illustrations of the different orientation relationships between laser beam and the inclined surfaces at edges/corners of the build plate, laser originates from the left side. The drawings refer to the scenario when a thin layer of powder has been applied, and the laser strikes at the edge of the scanned area of layer n. (a) illustrates the four conditions of surface orientation to the laser. (b), (c), (d), (e) are magnified sections of surface 1, 2, 3, 4 shown in (a), respectively. The layer n to be scanned by laser is encircled by red dashed lines. All the surfaces are built with 45° angle to the build plate, while surface 1, 2 are upskin surfaces and surface 3, 4 are downskin surfaces. Powder particles are assumed to be 30 μm in diameter, equal to the D50. Layer thickness is also 30 μm. The red curved arrows indicate the laser turns around as it reaches the edge of the scan area (blue dashed line). (For interpretation of the references to colour in this figure legend, the reader is referred to the web version of this article.)

area where the laser turns around must be different for the scenarios described in Fig. 16.

Furthermore, although commercial L-PBF systems employ F-theta lens [38] to ensure uniformity of beam shape and intensity across the build area, some inaccuracy is inevitable at the current stage. Therefore, the deviation of the laser beam intensity profile at the edges and corners of the build is also a factor in surface roughness.

4.2. Effects of gas flow and recoating process

The specimens exposed earlier and placed closer to the inlet generates by-products that affects the surface roughness of specimens exposed later and located in the path in which the by-products are directed. Meanwhile, as the three layers of specimens were stacked, there is an increase in build height, which also affects the surface roughness by changing the heat dissipation from the specimen during the building process [20]. Since the specimens are placed relatively far apart over X-Y plane in the experiment conducted (Fig. 2), stronger influence of exposure sequence is expected from a build with closer placement of specimens. Exposure of the specimen against the flow direction does not show a clear improvement to surface finish in the present study according to the neural network analysis for both upskin surfaces (compare Fig. 12a and c) and downskin surfaces (compare Fig. 13a and c). In an EOS M280 machine, the recoater operates from right to left while the gas flow operates in the perpendicular direction from the back to the front of the machine. The recoater has a sorting effect on powder delivery by particle size, fine particles (< 10 μm in diameter) are not carried past the right side of the build plate where the recoating starts [34]. Redeposited spatter particles with diameters larger than the layer thickness, if not fused by laser to the previous layer, can be carried by the recoater over a certain distance and affect roughness close to the powder overflow [39]. It is worth noting that flow velocity distribution is not symmetric about Y axis (Fig. 2) as the placement of hardware (recoater arm, overflow chamber, feedstock, etc) as boundary conditions of the flow establishment is not symmetric either. The contour plots of Ra value distribution (Fig. 12 and Fig. 13) generally show higher values close to the gas outlet (negative Y coordinate) and at left side of the build close to the powder overflow (negative X coordinate). These variations in Ra are combined effects of gas flow pattern in local velocity and direction and powder recoating.

4.3. Effect of build height

Although the effect of build height is convoluted with exposure sequence in the experiments, one can infer from the predictions by neural network under hypothetical conditions if the build height plays a role in forming surface roughness, based on the assumption that the neural network model provides good prediction. Heat dissipation away from the laser fusion zone becomes slower with increasing build height due to the lower thermal conductivity of the powder bed surrounding the specimen [20,21]. The increase in build height seems to benefit 60° upskin surface finish in both mean value and variance of Ra over the build area according to the neural network model (Fig. 14). One possible explanation is that the slower heat dissipation assists the interlayer wetting. However, this is not the case for 45° downskin (Fig. 15a), where melt pool extension dominates the surface roughness and a faster heat dissipation from the fusion zone is preferred [21].

The accumulation of spatter particles at the gas inlet and outlet can cause some change in the boundary conditions of the flow establishment over the course of the experiment and thus affect the efficiency of process by-product removal locally. The amount of spatter particles generated during L-PBF is dependent on the total area of exposure, the laser energy input and the atmosphere (oxygen content) in the processing chamber [40]. Noting that a moderate amount of spatter was generated as the specimens cover a considerable fraction of the build area (Fig. 1) and a standard processing recipe recommended by EOS was applied, the change of gas flow over time is considered as the secondary factor in the build height (Z) direction.

One can assume that the effect of recoating as described in Section 4.2 is consistent with increasing build height. The assumption is based on the observations that no significant thermal distortion took place while building the specimens and the recoater remained intact throughout the experiment.

5. Conclusions

For inclined surfaces of given orientations to the build plate, the influence of specimen location, build height and orientation to the centre of the build on surface roughness are investigated. The orientation of inclined surface to the build centre above which the laser originate shows a clear and repeatable influence: inclined surfaces that build up and towards the laser has smoother surface than those build up and away from the laser. This build-up orientation effect holds for both upskin and downskin surfaces that are fundamentally different in surface roughness formation [21,30] and becomes stronger as the inclined surface locates farther away from the laser beam origin.

The roughness results imply quality variation along the directions of three main operations, namely the directed shielding gas, the recoating and the build direction. A neural network regression model was built with the Ra data from a large number of experimented surfaces, predictions of surface roughness distribution in the 3D build volume of an EOS M280 machine are presented with predefined exposure sequence and surface orientation. At a given build height, higher surface roughness is generally expected from the left side (close to the powder overflow) and the front (close to the gas outlet) of the machine, which indicates the combined effects imposed by gas flow and recoating. The neural network model suggests changes in roughness value with build height (Fig. 14 and Fig. 15) and possible causes for the variation are discussed in detail with reference to previous works.

The physical measurements of process signatures such as uniformity of powder coating, gas flow, spatter generation and thermal field and their correlation with surface roughness are beyond the scope of the study but are suggested for future work. This pattern in which roughness varies in 3D has implications for improvements of hardware and software towards better intra-build quality consistency. For experimental optimisation of processing parameters to minimise surface roughness of L-PBF products, this paper can be used as a guide for design of specimen, specimen placement and orientation relative to the machine system.

CRediT authorship contribution statement

Zhuoer Chen: Conceptualization, Methodology, Formal analysis, Investigation, Writing - original draft, Writing - review & editing, Visualization. **Xinhua Wu**: Conceptualization, Supervision, Writing - review & editing, Funding acquisition. **Chris Davies**: Conceptualization, Supervision, Writing - review & editing, Funding acquisition.

Declaration of Competing Interest

The authors declare that they have no known competing financial interests or personal relationships that could have appeared to influence the work reported in this paper.

Acknowledgements

This work is funded by the Science & Industry Endowment Fund under the programme RP04-153 “Manufacturing a small demonstrator aero-engine entirely through additive manufacturing” and the Australia Research Council IH130100008 “Industrial Transformation Research Hub for Transforming Australia’s Manufacturing Industry through High Value Additive Manufacturing”. The support and assistance from Monash Centre for Election Microscopy (MCEM) is gratefully acknowledged.

References

[1] T. DebRoy, T. Mukherjee, J.O. Milewski, J.W. Elmer, B. Ribic, J.J. Blecher, W. Zhang, Scientific, technological and economic issues in metal printing and their solutions, Nat. Mater. 18 (2019) 1026–1032, https://doi.org/10.1038/s41563-019-0408-2.

[2] M. Megahed, H.W. Mindt, J. Willems, P. Dionne, L. Jacquemetton, J. Craig, P. Ranade, A. Peralta, LPBF right the first time—the right mix between modeling and experiments, Integr. Mater. Manuf. Innov. 8 (2019) 194–216, https://doi.org/10.1007/s40192-019-00133-8.

[3] J.A. Slotwinski, E.J. Garboczi, P.E. Stutzman, C.F. Ferraris, S.S. Watson, M.A. Peltz, Characterization of metal powders used for additive manufacturing, J. Res. Natl. Inst. Stand. Technol. 119 (2014) 460–493, https://doi.org/10.6028/jres.119.018.

[4] Z. Snow, R. Martukanitz, S. Joshi, On the development of powder spreadability metrics and feedstock requirements for powder bed fusion additive manufacturing, Addit. Manuf. 28 (2019) 78–86, https://doi.org/10.1016/j.addma.2019.04.017.

[5] R.J. Hebert, Viewpoint: metallurgical aspects of powder bed metal additive manufacturing, J. Mater. Sci. 51 (2016) 1165–1175, https://doi.org/10.1007/s10853-015-9479-x.

[6] E.J. Garboczi, N. Hrabe, Particle shape and size analysis for metal powders used for additive manufacturing: technique description and application to two gas-atomized and plasma-atomized Ti64 powders, Addit. Manuf. 31 (2020), 100965, https://doi.org/10.1016/j.addma.2019.100965.

[7] C. Meier, R. Weissbach, J. Weinberg, W.A. Wall, A.J. Hart, Critical influences of particle size and adhesion on the powder layer uniformity in metal additive manufacturing, J. Mater. Process. Technol. 266 (2019) 484–501, https://doi.org/10.1016/j.jmatprotec.2018.10.037.

[8] P. Bidare, I. Bitharas, R.M. Ward, M.M. Attallah, A.J. Moore, Fluid and particle dynamics in laser powder bed fusion, Acta Mater. 142 (2018) 107–120, https://doi.org/10.1016/j.actamat.2017.09.051.

[9] S.A. Khairallah, A.T. Anderson, A.M. Rubenchik, W.E. King, Laser powder-bed fusion additive manufacturing: physics of complex melt flow and formation mechanisms of pores, spatter, and denudation zones, Acta Mater. 108 (2016) 36–45, https://doi.org/10.1016/j.actamat.2016.02.014.

[10] A. Ladewig, G. Schlick, M. Fisser, V. Schulze, U. Glatzel, Influence of the shielding gas flow on the removal of process by-products in the selective laser melting process, Addit. Manuf. 10 (2016) 1–9, https://doi.org/10.1016/j.addma.2016.01.004.

[11] M.J. Matthews, G. Guss, S.A. Khairallah, A.M. Rubenchik, P.J. Depond, W.E. King, Denudation of metal powder layers in laser powder bed fusion processes, Acta Mater. 114 (2016) 33–42, https://doi.org/10.1016/j.actamat.2016.05.017.

[12] M. Schniedenharn, F. Wiedemann, J.H. Schleifenbaum, Visualization of the shielding gas flow in SLM machines by space-resolved thermal anemometry, Rapid Prototyp. J. 24 (2018) 1296–1304, https://doi.org/10.1108/RPJ-07-2017-0149.

[13] T.M. Wischeropp, C. Emmelmann, M. Brandt, A. Pateras, Measurement of actual powder layer height and packing density in a single layer in selective laser melting, Addit. Manuf. 28 (2019) 176–183, https://doi.org/10.1016/j.addma.2019.04.019.

[14] X.J. Wang, L.C. Zhang, M.H. Fang, T.B. Sercombe, The effect of atmosphere on the structure and properties of a selective laser melted Al-12Si alloy, Mater. Sci. Eng. A 597 (2014) 370–375, https://doi.org/10.1016/j.msea.2014.01.012.

[15] C. Pauzon, A. Leicht, U. Klement, P. Forêt, E. Hryha, Effect of the process gas and scan speed on the properties and productivity of thin 316L structures produced by laser-powder bed fusion, Met. Mater. Trans. A 51 (2020) 5339–5350, https://doi.org/10.1007/s11661-020-05923-w.

[16] B. Ferrar, L. Mullen, E. Jones, R. Stamp, C.J. Sutcliffe, Gas flow effects on selective laser melting (SLM) manufacturing performance, J. Mater. Process. Technol. 212 (2012) 355–364, https://doi.org/10.1016/j.jmatprotec.2011.09.020.

[17] A. Bin Anwar, Q.C. Pham, Selective laser melting of AlSi10Mg: effects of scan direction, part placement and inert gas flow velocity on tensile strength, J. Mater. Process. Technol. 240 (2017) 388–396, https://doi.org/10.1016/j.jmatprotec.2016.10.015.

[18] S. Ly, A.M. Rubenchik, S.A. Khairallah, G. Guss, M.J. Matthews, Metal vapor micro-jet controls material redistribution in laser powder bed fusion additive manufacturing, Sci. Rep. 7 (2017) 1–12, https://doi.org/10.1038/s41598-017-04237-z.

[19] S. Zhang, B. Lane, J. Whiting, K. Chou, On thermal properties of metallic powder in laser powder bed fusion additive manufacturing, J. Manuf. Process. 47 (2019) 382–392, https://doi.org/10.1016/j.jmapro.2019.09.012.

[20] M. Jamshidinia, R. Kovacevic, The influence of heat accumulation on the surface roughness in powder-bed additive manufacturing, Surf. Topogr. Metrol. Prop. 3 (2015), 014003, https://doi.org/10.1088/2051-672X/3/1/014003.

[21] A. Ilin, R. Logvinov, A. Kulikov, A. Prihodovsky, H. Xu, V. Ploshikhin, B. Günther, F. Bechmann, Computer aided optimisation of the thermal management during laser beam melting process, Phys. Procedia 56 (2014) 390–399, https://doi.org/10.1016/j.phpro.2014.08.142.

[22] F. Calignano, Design optimization of supports for overhanging structures in aluminum and titanium alloys by selective laser melting, Mater. Des. 64 (2014) 203–213, https://doi.org/10.1016/j.matdes.2014.07.043.

[23] D. Wang, Y. Yang, Z. Yi, X. Su, Research on the fabricating quality optimization of the overhanging surface in SLM process, Int. J. Adv. Manuf. Technol. 65 (2012) 1471–1484, https://doi.org/10.1007/s00170-012-4271-4.

[24] J.P. Bons, A review of surface roughness effects in gas turbines, J. Turbomach. 132 (2010) 1–16, https://doi.org/10.1115/1.3066315.

[25] P. Li, D.H. Warner, J.W. Pegues, M.D. Roach, N. Shamsaei, N. Phan, Towards predicting differences in fatigue performance of laser powder bed fused Ti-6Al-4V coupons from the same build, Int. J. Fatigue 126 (2019) 284–296, https://doi.org/10.1016/j.ijfatigue.2019.05.004.

[26] L. Newton, N. Senin, C. Gomez, R. Danzl, F. Helmli, L. Blunt, R. Leach, Areal topography measurement of metal additive surfaces using focus variation microscopy, Addit. Manuf. 25 (2019) 365–389, https://doi.org/10.1016/j.addma.2018.11.013.

[27] D. Dai, D. Gu, Tailoring surface quality through mass and momentum transfer modeling using a volume of fluid method in selective laser melting of TiC/AlSi10Mg powder, Int. J. Mach. Tools Manuf. 88 (2015) 95–107, https://doi.org/10.1016/j.ijmachtools.2014.09.010.

[28] I. Yadroitsev, I. Smurov, Surface morphology in selective laser melting of metal powders, Phys. Procedia 12 (2011) 264–270, https://doi.org/10.1016/j.phpro.2011.03.034.

[29] G.E. Bean, D.B. Witkin, T.D. McLouth, D.N. Patel, R.J. Zaldivar, Effect of laser focus shift on surface quality and density of Inconel 718 parts produced via selective laser melting, Addit. Manuf. 22 (2018) 207–215, https://doi.org/10.1016/j.addma.2018.04.024.

[30] G. Strano, L. Hao, R.M. Everson, K.E. Evans, Surface roughness analysis, modelling and prediction in selective laser melting, J. Mater. Process. Technol. 213 (2013) 589–597, https://doi.org/10.1016/j.jmatprotec.2012.11.011.

[31] J. Trapp, A.M. Rubenchik, G. Guss, M.J. Matthews, In situ absorptivity measurements of metallic powders during laser powder-bed fusion additive manufacturing, Appl. Mater. Today 9 (2017) 341–349, https://doi.org/10.1016/j.apmt.2017.08.006.

[32] S. Kleszczynski, A. Ladewig, K. Friedberger, J. zur Jacobsmühlen, D. Merhof, G. Witt, Position dependency of surface roughness in parts from laser beam melting systems, in: Proceedings of the 26th Internation Solid Free Form Fabrication (SFF) Symposium 2015, 2015, pp. 360–370.

[33] S. Rott, A. Ladewig, K. Friedberger, J. Casper, M. Full, J.H. Schleifenbaum, Surface roughness in laser powder bed fusion – Interdependency of surface orientation and laser incidence, Addit. Manuf. 36 (2020), 101437, https://doi.org/10.1016/j.addma.2020.101437.

[34] Z. Chen, X. Wu, D. Tomus, C.H.J. Davies, Surface roughness of Selective Laser Melted Ti-6Al-4V alloy components, Addit. Manuf. 21 (2018) 91–103, https://doi.org/10.1016/j.addma.2018.02.009.

[35] International Organization for Standardardization, ISO 4287:1997 Geometrical prodcut specifications (GPS) - surface texture: profile method - terms, definitions and surface texture parameters, first ed., Geneva, 1997.

[36] M. Leary, Surface Roughness Optimisation for Selective Laser Melting (SLM): Accommodating Relevant and Irrelevant Surfaces, Elsevier Ltd, 2017, https://doi.org/10.1016/B978-0-08-100433-3.00004-X.

[37] Y. Tian, D. Tomus, A. Huang, X. Wu, Melt pool morphology and surface roughness relationship for direct metal laser solidification of Hastelloy X, RPJ 26 (2020) 1389–1399, https://doi.org/10.1108/RPJ-08-2019-0215.

[38] K. Godineau, S. Lavernhe, C. Tournier, Calibration of galvanometric scan heads for additive manufacturing with machine assembly defects consideration, Addit. Manuf. 26 (2019) 250–257, https://doi.org/10.1016/j.addma.2019.02.003.

[39] M. Taheri Andani, R. Dehghani, M.R. Karamooz-Ravari, R. Mirzaeifar, J. Ni, Spatter formation in selective laser melting process using multi-laser technology, Mater. Des. 131 (2017) 460–469, https://doi.org/10.1016/j.matdes.2017.06.040.

[40] Y. Liu, Y. Yang, S. Mai, D. Wang, C. Song, Investigation into spatter behavior during selective laser melting of AISI 316L stainless steel powder, Mater. Des. 87 (2015) 797–806, https://doi.org/10.1016/j.matdes.2015.08.086.